Research Square

Preprints are preliminary reports that have not undergone peer review.
They should not be considered conclusive, used to inform clinical practice,
or referenced by the media as validated information.

Residual Stress and Shape Distortion Management in Polymer Printing of Thin-walled Complex Geometries

Anastasia Muliana

amuliana@tamu.edu

Texas A&M University

Research Article

Keywords: Additive Manufacturing, Thin-walled structures, PLA, FEA Simulation

Posted Date: July 9th, 2026

DOI: https://doi.org/10.21203/rs.3.rs-9808390/v1

License: This work is licensed under a Creative Commons Attribution 4.0 International License.
Read Full License

Additional Declarations:
No competing interests reported.

Declaration of interests

The authors declare that they have no known competing financial interests or personal relationships that could have appeared to influence the work reported in this paper.

The authors declare the following financial interests/personal relationships which may be considered as potential competing interests:

Version of Record: A version of this preprint was published at Progress in Additive Manufacturing on September 11th, 2026. See the published version at https://doi.org/10.1007/s40964-026-01947-7.

Residual Stress and Shape Distortion Management in Polymer Printing of Thin-walled Complex Geometries

Abstract

Residual stress developed during fused deposition modeling (FDM) printing of thermoplastic polymers can lead to severe shape distortion in thin-walled complex geometries, limiting dimensional accuracy and structural integrity. This study presents FDM printing and its digital twin to investigate the thermo-mechanical mechanisms governing warpage, wrinkling, and residual stress formation during FDM printing. The printing simulation maps the exact layer-by-layer deposition process using a trajectory-based event series coupled with transient heat transfer and stress analyses, which generate a digital twin of FDM printing. The simulation incorporates progressive material activation, moving heat sources, temperature-dependent thermal and elastic-plastic properties to account for phase transformation during solidification, and evolving thermal boundary conditions associated with convection, radiation, and conduction. The simulation was validated to predict wrinkling and warpage of thin-walled cubes and tessellated tubes out of polylactic acid (PLA), measured using high-resolution 3D scanning, capturing both the magnitude and spatial distribution of shape distortion. The validated digital twin model of FDM printing provides a predictive tool for optimizing printing parameters, understanding residual stress formation, and improving the manufacturability of thin-walled complex polymer structures.

1. Introduction

Polymer manufacturing, including Fused Deposition Modeling (FDM), involves melting and solidifying polymers, governed by thermal and mechanical processes. During processing, the chemical, mechanical, and thermal properties and dimensions of the polymer gradually change, and together with the changes in boundary conditions, they result in the formation of residual stresses. Compressive residual stress in thermoplastic polymers can inhibit crack growth and enhance fatigue strength (Chaoui et al. 1987 and Hornberger and Devries 1987); however, residual stress can also induce the warpage and distortion of the shape (Hakimian and Sulong 2012).

Specifically, for the FDM of thermoplastic polymers, the process involves multiple and repeated thermal cycles, starting from feeding the filament or pellets through a heated nozzle above the polymer's melting temperature (T_m). As the polymer melt (extrudate) leaves the nozzle, it begins to cool to a lower ambient temperature below the glass transition temperature (T_g) and solidifies. The melting and flow of polymers as they pass through hot ends influence bonding during printing (Xia et al., 2018a and b, Mishra et al., 2021, Ufodike and Nzebuka, 2022, and Nzebuka et al., 2022). The repeated deposition of beads during the printing process introduces cyclic thermal profiles with decaying behavior due to convection and radiation with the environment, as well as thermal conduction with adjacent beads and the print bed, generating temporal and spatially dependent heat fluxes throughout each bead (Vaes et al., 2019). These thermal profiles cause different deformations in the bead that is being deposited and the adjacent deposited beads, which can result in the formation of residual stress and shape distortion.

Additive manufacturing (AM) techniques, such as FDM, have been increasingly used to create structures of complex geometries out of thermoplastic polymers, for numerous applications ranging from automotive, healthcare, space, and defense sectors, as well as in art and craft

industries. One of the shortcomings of the thermoplastic FDM is the challenge in achieving geometrical accuracy, which is often seen in the formation of warpage, wrinkling, and shape distortion. This geometrical inaccuracy, which is attributed to the formation of residual (thermal) stresses, is a material and geometric specific (Spoerk et al., 2020). For instance, for polymers with high viscosities, higher nozzle temperatures are needed to extrude the melt (Spoerk et al., 2018), which can increase the thermal gradient with the surrounding environment, hence increasing the residual stresses. This issue can be addressed by increasing the bed and environment temperatures during the printing, followed by cooling down the printed object to an ambient temperature. For polymers with a low degree of crystallinity, nonuniform shrinkage can induce warpage, which can be overcome by reducing the printing rate. In commercially available filaments, such as polylactic acid (PLA) and acrylonitrile butadiene styrene (ABS), where they can be printed without noticeable shape distortion for most parts, shape distortion can still occur, particularly in thin-walled structures and complex (nonlinear) shapes. As discussed in Spoerk et al. (2020), changing the processing conditions can potentially address the issue related to geometrical inaccuracy in polymer printing. However, these processing parameters are not universal as they depend on the materials and geometries of the printed objects.

Modeling and simulation of the FDM process have been widely considered to describe the physics of the printing process at various processing stages and understand the influence of printing factors, materials, and geometries on the quality of the printed objects (Al Rasid and Koc 2021). Several models have focused on describing the heat transfer processes during filament deposition and the formation of adhesive bonding between the layer depositions from thermal sintering, e.g., Yardimci et al., 1997, Costa et al., 2017, Garzon-Hernandez et al., 2020. The adhesion strength, bonded areas, and void contents predicted by the models could describe the

variations in the overall elastic stiffness and strength of the 3D printed objects at varying printing conditions, including layer height, printing speed, nozzle temperature, and environmental temperature. However, this approach is limited in describing residual stress and shape distortion.

The core reason for the formation of residual stress and shape distortion is the nonuniform deformations from thermal strain and shrinkage during solidification and cooling of the polymer. Large structures are more susceptible to nonuniform deformations, causing large deformation gradients. In thin-walled structures, deformation gradients can occur in multiple directions, both in-plane and through the thickness, contributing to more complex shape distortion than simple bending that can be predicted by analytical solutions. To describe the residual stress and shape distortion in the FDM process, several analytical models have incorporated the thermal expansion coefficient to couple the heat transfer and mechanical deformation, e.g., Wang et al., 2007, Xinhua et al., 2015. While this approach can qualitatively describe the formation of warpage and the influence of thermal gradients on the severity of warpage, it is limited in predicting the magnitude of warpage. This limitation is attributed to ignoring gradual changes in the chemical, thermal, and mechanical properties as the polymer solidifies, neglecting the dimension and shape changes of the polymer extrudate, and oversimplifying the constitutive material models for the polymer.

Several attempts have been made to improve the FDM simulation by incorporating various thermo-mechanical processes. Akbar et al. (2022) investigated the formation of warpage generated during the printing process of shape memory polymer. They introduced coupled heat transfer and thermo-elastic deformation with thermal and mechanical properties of the polymer extrudate varying with temperatures to simulate the phase transformation of the polymer. By optimizing printing factors, they could reduce the residual stress and warpage by 80%. Other studies have shown that incorporating viscoelastic models instead of elastic models yielded more accurate

predictions of the shape and dimension changes of polymer extrudate during deposition (Xia et al., 2019) and residual stresses (Duty et al., 2018; Sreejith et al., 2021). The phase transformation of polymer melts during printing can induce crystallization as the polymer solidifies, affecting the mechanical properties of the printed objects, as discussed by Brenken et al. (2018, 2019) and Jiang et al. (2023). An alternative modeling approach to account for irreversible changes in the material properties as the polymer solidifies is to describe the deformation of the polymer with elastic-plastic models, e.g., Armillotta et al., 2018, and El Moumen et al., 2019. This approach gave a reasonably good prediction of the warpage of the printed object.

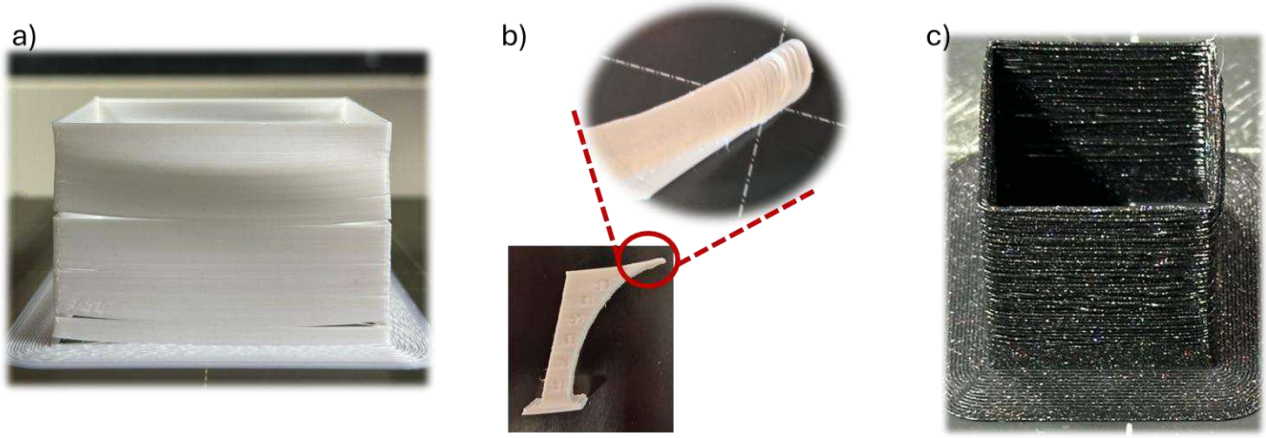


Figure 1: Shape distortions in 3D printed polymers: a) warpage and layer separation of a thin-walled cube, b) sagging and stringing of an overhang, and c) warpage and wrinkling of a thin-walled cube

In this paper, we present a combined simulation and experiment of FDM printing to understand the key printing parameters and physical mechanisms that contribute to shape distortions in polymer printing of thin-walled complex geometries. Several common shape distortions include warpage, layer separation, wrinkling, and stringing, as depicted in **Fig. 1**. This understanding can help select optimized printing parameters to minimize shape distortions in polymer printing of thin-walled complex geometries. We map the exact layer-by-layer deposition process during printing and incorporate heat transfer and deformation as the polymer solidifies to

perform a digital twin of FDM printing, which is discussed in **Section 2**. We present model validation and a parametric study to explore the influence of printing parameters and identify the mechanisms that contribute to shape distortions in thin-walled cubes in **Section 3**. Using the simulation, we optimize the printing parameters to print a thin-walled tessellation structure that is comprised of overhang walls, another challenge in printing thin-walled structures, which is presented in **Section 4**. Finally, we conclude and discuss future directions in **Section 5**.

2. Digital Twin Modeling of FDM Process

Duty et al. (2018) defined the printability of polymers by the ability to (i) be extruded through a nozzle, (ii) retain its shape post-extrusion, (iii) bridge a defined gap, and (iv) maintain geometric stability upon cooling. These criteria are largely governed by the polymer's rheological properties, such as melt viscosity and flow behavior. Understanding the relationship between process parameters and material properties helps optimize printing for specific applications (Solomon et al., 2021). The effect of the printing parameters (e.g., nozzle diameter, nozzle temperature, bed temperature, environment temperature, and printing speed, layer thickness, raster width, infill density, and infill pattern) on the layer adhesion and mechanical properties of printed objects is well-documented, from both experimental and numerical methods (Popescu et al., 2018).

Herein, we present a simulation that maps the exact layer depositions during printing, which is crucial for determining the formation of residual stress and warpage. The simulation involves a transient heat transfer analysis followed by a transient stress analysis, where the temperature profiles are used as thermal loads in the stress analysis. We developed a trajectory-based motion tracking of the hot end through a series of events, which includes time (t), positions $\mathbf{r}(x, y, z)$, and amplitude values of materials and field variables, as shown in **Fig. 2**. For solving the thermal and deformation governing equations, we used ABAQUS FE analysis with AM Modeler.

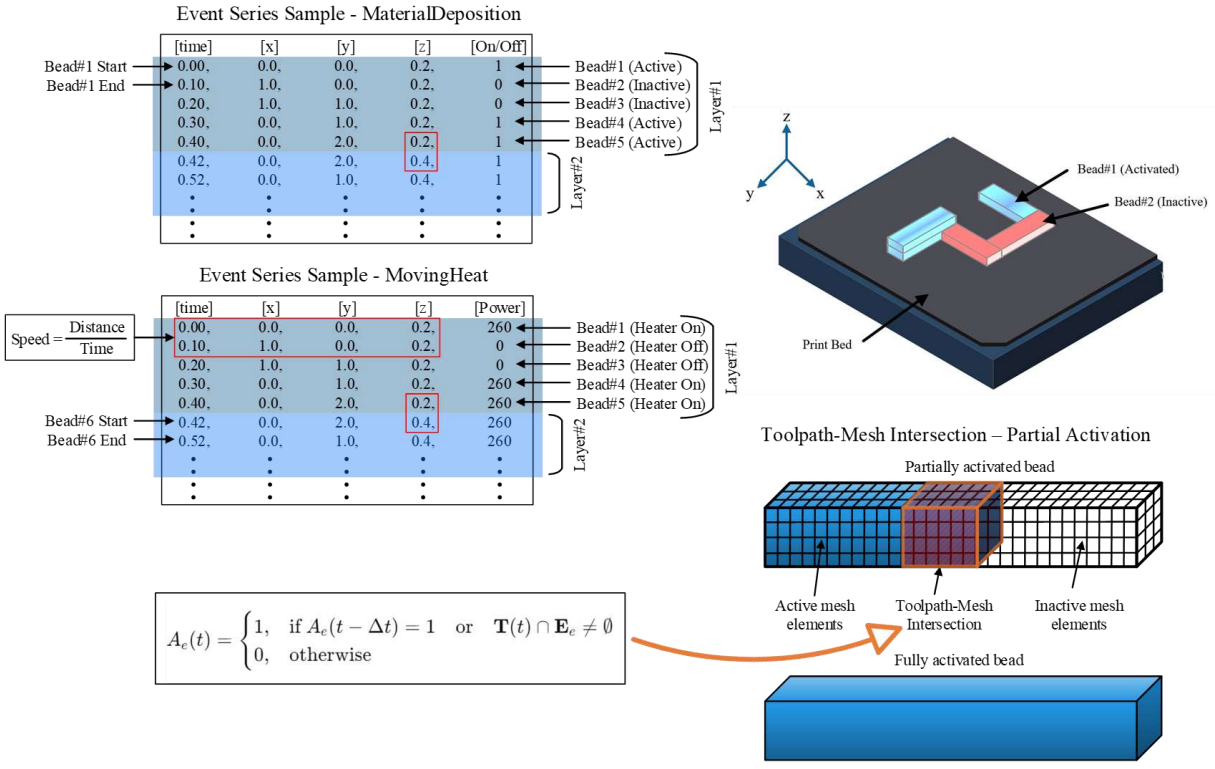


Figure 2: Event-based toolpath-mesh intersection model used for progressive element activation.

The event series controls both the material input source and the heat source. The material input source is modeled through the "MaterialDeposition" event series, with an amplitude value of either '1' (indicating material extrusion) or '0' (indicating no material extrusion). The heat source, representing the heating element, is governed by the "MovingHeat" event series, with the amplitude value corresponding to the heating power. The combination of these event series enables precise control of both the material deposition and thermal input during the simulation (depicted in **Figure 3**). The speed of the hot end is controlled by adjusting the time required to execute a specific event in the event series. The time for moving the hot end is calculated by dividing the total distance traveled in a three-dimensional (3D) space by the desired speed.

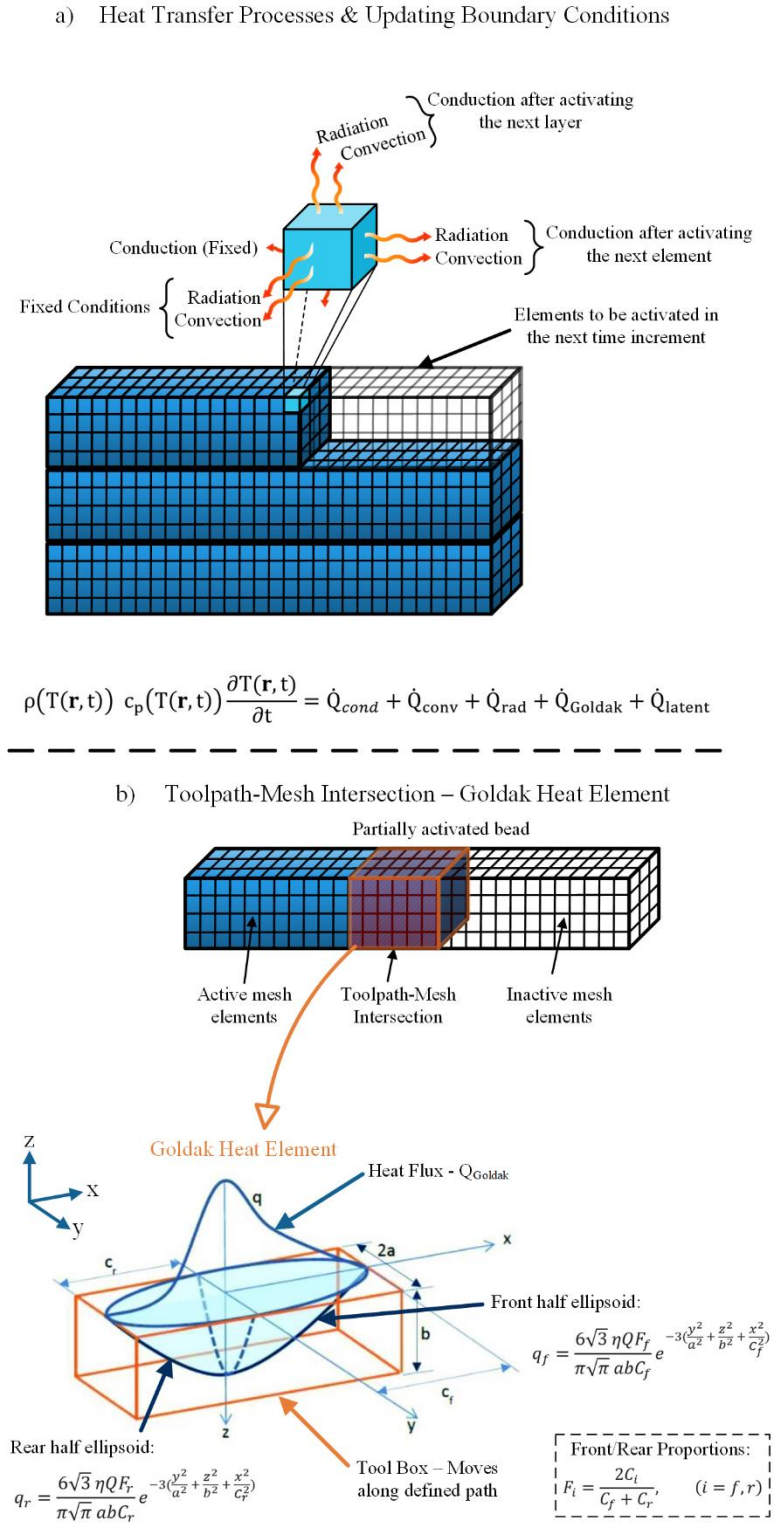


Figure 3: Event-based modeling for the (a) heat transfer process and updating boundary conditions, and (b) the motion of a Goldak heating element along the toolpath**.**

The transient heat transfer analysis consists of 1) progressive mesh element activation to simulate the deposition of new material as the hot end moves, 2) progressive heating of the deposited material by a moving heat source, and 3) transient cooling of the deposited material through conduction, convection, and radiation. The radiation is modeled between the deposited mesh and (1) the surrounding environment (set at room temperature), and (2) other deposited meshes. The thermal boundary of the deposited material continuously changes. The material is activated immediately upon deposition on the print bed, which is in a molten state. A temperature gradient in the deposited beads is due to convection with the environment in the standoff region (Santos et al. 2023). To capture this temperature profile, the mesh elements were activated at a uniform temperature slightly lower than the nozzle temperature (T_n), while a heat source with a minor intensity was applied to raise the temperature to match the nozzle's temperature, using a Goldak heating profile (Nascimento et al. 2023). The Goldak profile is used to describe the heat input distribution in processes, represented by a three-dimensional, elongated double ellipsoidal equation (see **Fig. 3b**). Upon the activation of new mesh elements, some of the previously activated free surfaces transition into internal surfaces, while new free surfaces are created.

2.1 Transient heat transfer analysis

The thermal analysis is governed by the following rate of temperature change:

$$\rho\big(\mathrm{T}(\mathbf{r},\mathrm{t})\big)\ \mathrm{c_p}\big(\mathrm{T}(\mathbf{r},\mathrm{t})\big)\frac{\partial \mathrm{T}(\mathbf{r},\mathrm{t})}{\partial \mathrm{t}} = \dot{\mathrm{Q}}_{cond} + \dot{\mathrm{Q}}_{\mathrm{conv}} + \dot{\mathrm{Q}}_{\mathrm{rad}} + \dot{\mathrm{Q}}_{\mathrm{Goldak}} + \dot{\mathrm{Q}}_{\mathrm{latent}} \qquad (1)$$

where $\mathrm{c_p}\big(\mathrm{T}(\mathbf{r},\mathrm{t})\big)$ and $\rho\big(\mathrm{T}(\mathbf{r},\mathrm{t})\big)$ are the specific heat and density, respectively, whose values vary with temperature as the melt solidifies. Multiple thermal processes come into play. The first is a conduction, where $\dot{\mathrm{Q}}_{\mathrm{cond}}(\mathbf{r},\mathrm{t})$ is the conductive heat transfer rate per unit volume within a mesh element at location $\mathbf{r}(\mathrm{x},\mathrm{y},\mathrm{z})$ and time t, and is modeled as:

$$\dot{Q}_{cond}(\mathbf{r},t) = -\nabla \cdot \left(k\big(T(\mathbf{r},t)\big) \cdot \nabla T(\mathbf{r},t)\right) \cdot H(\mathbf{r},t-t_0) \quad (2)$$

where ∇ is the gradient operator in 3D space, $k\big(T(\mathbf{r},t)\big)$ is a temperature-dependent thermal conductivity tensor. To manage the activation of conduction as surfaces change, the Heaviside step function $H(\mathbf{r},t-t_0)$ controls the activation of thermal conduction at specific surfaces when they transition from free to internal surfaces, upon the activation of new elements at a time t_0. The Heaviside step function is defined as:

$$H(\mathbf{r},t-t_i) = \begin{cases} 1, & t \geq t_i \text{ and } \mathbf{r} \in \Omega \\ 0, & otherwise \end{cases} \quad (3)$$

where Ω represents the spatial domain representing the surfaces of activated mesh elements, where the Heaviside function is applied to represent thermal conduction. For each mesh element, time instances t_i are defined based on the changing boundary conditions caused by the progressive activation of new elements. The time instances ensure that the thermal conduction boundary condition is correctly modeled for evolving surfaces as the simulation progresses.

The second thermal process is convection, which describes heat loss through free convection at the exposed surfaces of the mesh elements:

$$\dot{Q}_{conv}(\mathbf{r},t) = -\frac{A_{conv}(\mathbf{r},t)}{V} \cdot h \cdot (T(\mathbf{r},t) - T_\infty) \cdot [H(\mathbf{r},t-t_0) - H(\mathbf{r},t-t_1)] \quad (4)$$

where $\dot{Q}_{conv}(\mathbf{r},t)$ is the convective heat transfer rate per unit volume, $A_{conv}(\mathbf{r},t)$ is the area of the free surface for a mesh element, V is the volume of a mesh element, h is the convective heat transfer coefficient at the free surface (also known as the film coefficient), and T_∞ is the temperature of the surrounding environment. Two Heaviside step functions are introduced to track changes between free and internal surfaces of the mesh elements. The first Heaviside function $H(\mathbf{r},t-t_0)$ activates the free convection process when a free surface forms at time t_0 due to element activation.

The second function, $\mathrm{H}(\mathbf{r}, \mathrm{t} - \mathrm{t}_1)$, deactivates convection when the free surface becomes an internal surface at time t_1, upon the activation of a subsequent element.

The third process is radiation heat transfer, which is considered the main contributor for heat transfer in the first 5-10 seconds post-deposition, given as:

$$\dot{\mathrm{Q}}_{\mathrm{rad}}(\mathbf{r}, \mathrm{t}) = -\frac{\mathrm{A}_{\mathrm{rad}}(\mathbf{r},\mathrm{t})}{\mathrm{V}} \cdot \epsilon \cdot \sigma \cdot \left(\mathrm{T}(\mathbf{r}, \mathrm{t})^4 - \mathrm{T}_\infty{}^4\right) \cdot [\mathrm{H}(\mathbf{r}, \mathrm{t} - \mathrm{t}_0) - \mathrm{H}(\mathbf{r}, \mathrm{t} - \mathrm{t}_1)] \qquad (5)$$

where $\dot{\mathrm{Q}}_{\mathrm{rad}}(\mathbf{r}, \mathrm{t})$ is the radiative heat transfer rate per unit volume, $\mathrm{A}_{\mathrm{rad}}(\mathbf{r}, \mathrm{t})$ denotes the free surface area of a mesh element, ϵ is the emissivity of the material's surface, σ is the Stefan-Boltzmann constant. Like the convection process, two Heaviside step functions are used to account for the evolution of boundary conditions.

The fourth process is the Goldak heating, where $\dot{\mathrm{Q}}_{\mathrm{Goldak}}$ is the volumetric heat absorption rate representing the heat added to a mesh element from the hot end with a Goldak heating profile as described in **Fig. 3**, and finally, $\dot{\mathrm{Q}}_{\mathrm{latent}}$ is accounts for the latent heat of fusion, calculated as:

$$\dot{\mathrm{Q}}_{latent}(\mathbf{r}, \mathrm{t}) = \rho\big(\mathrm{T}(\mathbf{r}, \mathrm{t})\big)\, \boldsymbol{L_f}\, \frac{\partial f_s(\mathrm{T}(\mathbf{r},\mathrm{t}))}{\partial \mathrm{t}} \qquad (6)$$

$$f_s(\mathrm{T}(\mathbf{r}, \mathrm{t})) = \begin{cases} 0, & T \geq T_l \\ \frac{T_l - T(\mathbf{r},\mathrm{t})}{T_l - T_s}, & T_s < T < T_l \\ 1, & T \leq T_s \end{cases} \qquad (7)$$

where L_f is the latent heat of fusion, $f_s(\mathrm{T}(\mathbf{r}, \mathrm{t}))$ is the phase fraction function describing the fraction of a mesh element that is in the solid phase, T_s is the solidus temperature of a material, and T_l is the liquidus temperature of a material. The latent heat of fusion is considered to track the solid-liquid interface within the deposited beads using the phase fraction function. This function allows for the modeling of phase changes (solidification) as the average temperature of a mesh element decreases to a value between the solidus and liquidus temperatures.

The field outputs from the thermal simulation, such as nodal temperature, temperature gradients, and heat flux, are calculated based on the heat transfer between adjacent mesh elements (both those representing the deposited polymer and the print bed). The field outputs from the thermal analysis are then input into a transient stress analysis, as discussed below.

2.2 Transient stress analysis

This stress analysis uses the previously calculated profiles for progressive element activation, solidification, heat fluxes, and nodal temperatures, discussed previously by Chen et al. (2023). We consider an elastic-plastic material model to account for irreversible changes in the mechanical properties of polymer solidification during printing. The present stress simulation does not account for stress relaxation or creep of the polymers. We neglect the shape evolution of the deposited beads over time, caused by viscous effects before solidification and the relaxation of thermal stress during cooling. To overcome such a limitation, the effect of melt solidification is captured by assigning an initial temperature, known as the relaxation temperature (T_{relax}), above which thermal straining generates negligible thermal stresses, following a previous study by An et al. (2021). This approach allows for a more manageable computational cost while still capturing the key thermal effects that influence stress development during and after deposition.

The stress analysis is governed by the following equilibrium equation:

$$\nabla \cdot \sigma(\mathbf{r}, t) + f(\mathbf{r}, t) = 0 \tag{8}$$

where $\nabla \cdot \sigma(\mathbf{r}, t)$ is the divergence of the stress tensor, which represents internal forces, and $f(\mathbf{r}, t)$ is the body force vector per unit volume (e.g., gravitational forces). A quasi-static loading is assumed. We consider a linearized strain measure, given by the following equation:

$$\epsilon(\mathbf{r}, t) = \frac{1}{2}\left(\nabla u(\mathbf{r}, t) + \left(\nabla u(\mathbf{r}, t)\right)^{T}\right) \tag{9}$$

where $\mathrm{u}(\mathbf{r},\mathrm{t})$ is the displacement vector field, and $\nabla\mathrm{u}(\mathbf{r},\mathrm{t})$ is its gradient. The total strain is calculated as the sum of the mechanical $\epsilon_{\mathrm{mechanical}}(\mathbf{r},\mathrm{t})$ and thermal $\epsilon_{\mathrm{thermal}}(\mathbf{r},\mathrm{t})$ strains:

$$\epsilon\,(\mathbf{r},\mathrm{t}) = \epsilon_{\mathrm{mechanical}}(\mathbf{r},\mathrm{t}) + \epsilon_{\mathrm{thermal}}(\mathbf{r},\mathrm{t}) \tag{10}$$

By assuming perfect plasticity with isotropic elastic behavior, the stress is given below:

$$\epsilon_{\mathrm{elastic}}(\mathbf{r},\mathrm{t}) = \epsilon(\mathbf{r},\mathrm{t}) - \epsilon_{\mathrm{plastic}}(\mathbf{r},\mathrm{t}) - \epsilon_{\mathrm{thermal}}(\mathbf{r},\mathrm{t}) \tag{11}$$

$$\sigma(\mathbf{r},\mathrm{t}) = \lambda(\mathbf{r},\mathrm{t}) \cdot \mathrm{tr}(\epsilon_{\mathrm{elastic}}(\mathbf{r},\mathrm{t})) \cdot \mathrm{I} + 2\mu(\mathbf{r},\mathrm{t}) \cdot \epsilon_{\mathrm{elastic}}(\mathbf{r},\mathrm{t}) \tag{12}$$

$$\lambda = \frac{E(\mathbf{r},\mathrm{t})\,\nu(\mathbf{r},\mathrm{t})}{(1+\nu(\mathbf{r},\mathrm{t}))(1-2\nu(\mathbf{r},\mathrm{t}))} \tag{13}$$

$$\mu(\mathbf{r},\mathrm{t}) = \frac{E(\mathbf{r},\mathrm{t})}{2(1+\nu(\mathbf{r},\mathrm{t}))} \tag{14}$$

where $\sigma(\mathbf{r},\mathrm{t})$ is the Cauchy stress tensor for a mesh element at location $\mathbf{r}$ and time t, $\lambda(\mathbf{r},\mathrm{t})$ and $\mu(\mathbf{r},\mathrm{t})$ are Lame's parameters relating the elastic modulus and Poisson's ratio, and $\mathrm{tr}(-)$ is the trace operator. The yield stress is modeled as temperature-dependent, $\sigma_y(\mathrm{T}(\mathbf{r},\mathrm{t}))$.

The thermal strain generated due to heating and cooling is modeled as:

$$\epsilon_{\mathrm{thermal}}(\mathbf{r},\mathrm{t}) = \alpha\big(\mathrm{T}(\mathbf{r},\mathrm{t})\big) \cdot \Delta\mathrm{T}(\mathbf{r},\mathrm{t}) \tag{19}$$

$$\Delta\mathrm{T}(\mathbf{r},\mathrm{t}) = \mathrm{T}(\mathbf{r},\mathrm{t}) - \mathrm{T}(\mathbf{r},0) \tag{20}$$

where $\alpha(\mathrm{T}(\mathbf{r},\mathrm{t}))$ is the temperature-dependent second-order thermal expansion tensor.

The mechanical response is evaluated to estimate residual stresses and shape distortion immediately after deposition and up to the end state, after the printed part cools to room temperature. Since the temperature profiles drive stress analysis, temperature-dependent mechanical properties are essential for achieving accurate stress results. The mechanical behavior is characterized by several properties: density $\rho\big(\mathrm{T}(\mathbf{r},\mathrm{t})\big)$, elastic modulus $E(\mathrm{T}(\mathbf{r},\mathrm{t}))$, Poisson's ratio $\nu(\mathrm{T}(\mathbf{r},\mathrm{t}))$, yield stress $\sigma_y(\mathrm{T}(\mathbf{r},\mathrm{t}))$, corresponding plastic strain $\varepsilon_y(\mathrm{T}(\mathbf{r},\mathrm{t}))$, and the coefficient of thermal expansion $\alpha(\mathrm{T}(\mathbf{r},\mathrm{t}))$.

3. Printing of Thin-walled Cubes

We assessed the capability and accuracy of the simulated FDM process by 3D printing thin-walled cubes using PLA filaments. Two thin-walled cubes, with a wall thickness of 0.4 mm and side lengths of 20 mm and 40 mm, were examined for their shape distortion through a combined simulation and experiment. The generated CAD models were simultaneously used for determining the slicing parameters in G-code and event series in FE analysis, as shown in **Fig. 4**. The slicing script obtained from the G-code was used as an event series (**Fig. 2**) to match the simulated layer deposition with the deposition during printing. The simulation and experimental printing consist of three steps: 1) layer deposition during printing of cubes, 2) holding period at a bed temperature to allow for complete solidification of cubes, and 3) cooling down the system to room temperature. The printed cubes were then scanned to examine any shape distortion by comparing the scanned geometry of the printed cubes with the original CAD models. These measurements were then compared with the simulated values of shape distortion. This comparison provided an insight into how well the simulation captured the physical deformation of the printed cubes, offering a means to explain the cause of shape distortions and determine mitigation strategies.

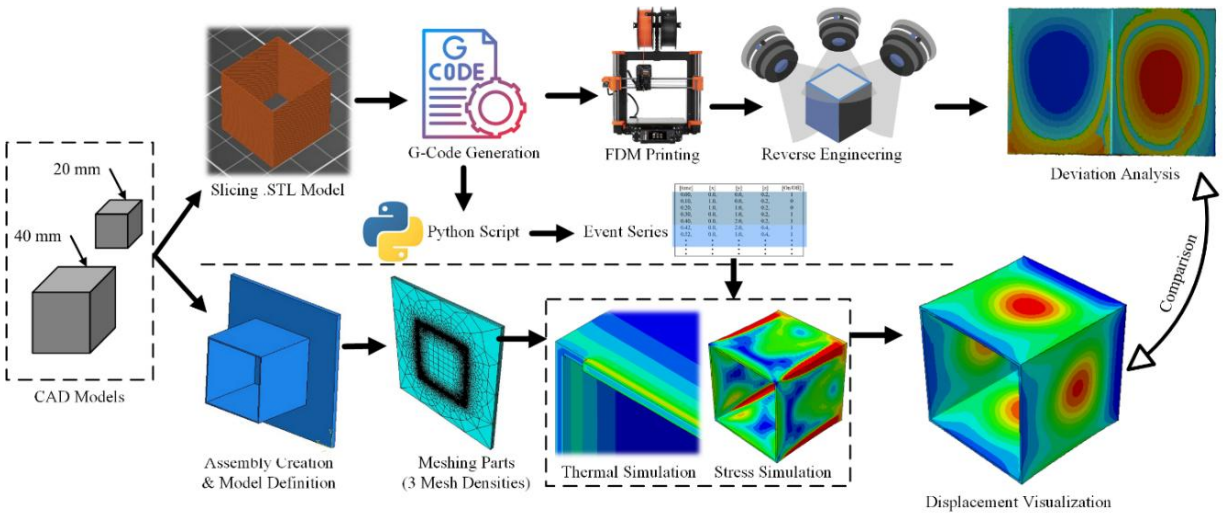


Figure 4: A simulation and experimental integration to evaluate shape distortion.

3.1 Material properties of PLA and reference printing parameters

The thermal conductivity, specific heat capacity, and coefficient of thermal expansion for the black PLA filament were experimentally measured using Laser Flash Analysis (LFA), Differential Scanning Calorimetry (DSC), and Thermomechanical Analysis (TMA), respectively. The remaining material properties for the black PLA filament were estimated based on the average properties of PLA reported in the literature (Ozen et al. 2022, Zhou et al. 2016, Kaavesina et al. 2012, Luo et al. 2022, Ronca et al., 2022, Prada et al., 2022, and Bhandari and Lopez-Anido 2020). A constant Poisson's ratio of 0.34 was used for PLA, as reported by (Ozen et al. 2022), and all properties were sampled at the same temperature intervals, except for specific heat capacity, which was sampled at a higher rate to accurately capture the thermal transitions. By analyzing the DSC curve, the solidus and liquidus temperatures of PLA were determined to be approximately 150 °C and 180 °C, respectively, while the latent heat of fusion was calculated to be around 25.4 kJ/kg. All thermal properties were defined over the temperature range of 20 °C to 200 °C, whereas the mechanical properties were specified between 20 °C and 150 °C. The choice of 150 °C as the relaxation temperature is supported by the onset of the melting peak in the DSC curve for PLA. **Figure 5** illustrates the temperature-dependent properties of PLA as it is heated through its glass transition and melting temperatures.

The material properties of the spring steel print bed were obtained from the literature (AISI 9260 61SICR7, Iron Alloy, Li et al., 2023), summarized in **Table 1.** They are assumed to be temperature independent within the printing temperature range (25 °C to 180 °C). The properties of PLA and the print bed will be used in the simulation discussed in **Section 3.2**.

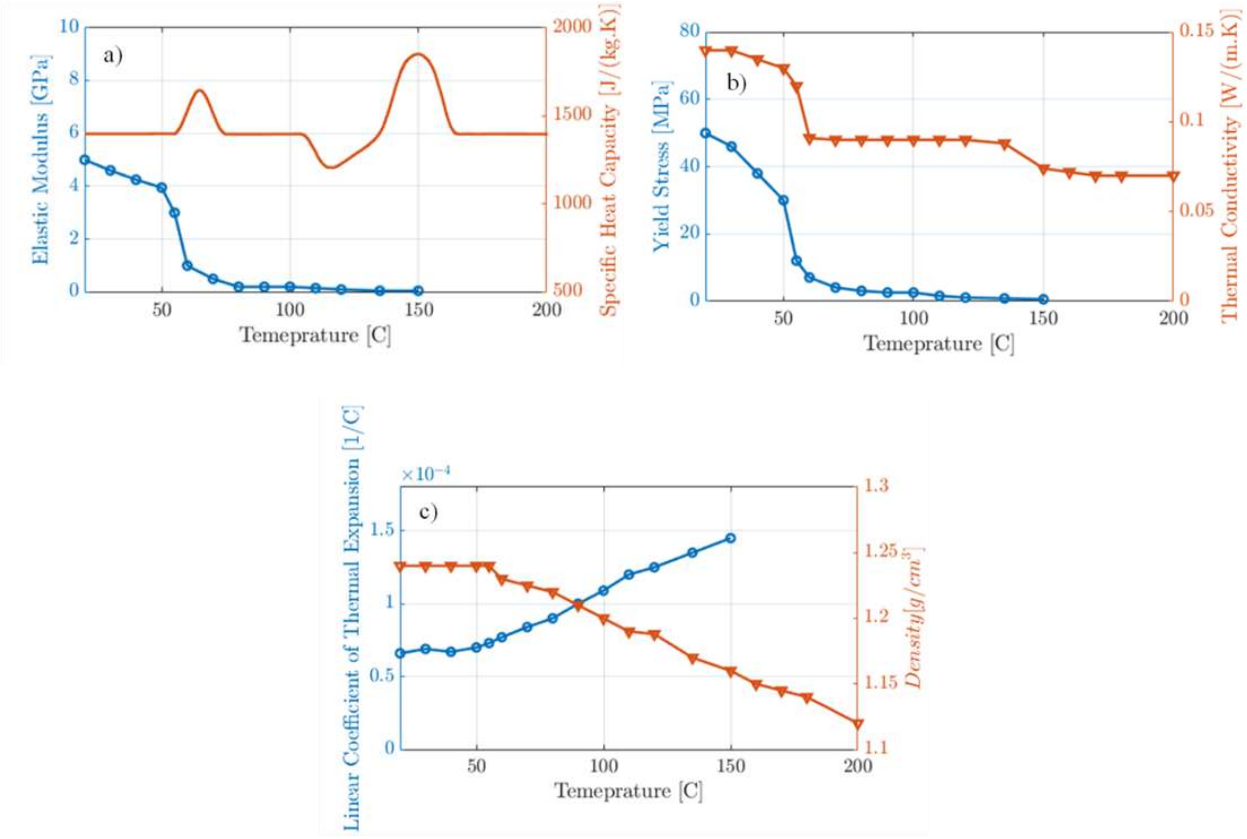


Figure 5: PLA thermal and mechanical time-dependent properties used in the simulations: (a) specific heat capacity (measured) and elastic modulus (Ozen et al. 2022, Zhou et al. 2016, Kaavesina et al. 2012), (b) thermal conductivity (measured) and yield strength (Luo et al. 2022, Ronca et al. 2022), and (c) density (Prada et al., 2022, and Bhandari and Lopez-Anido 2020) and linear coefficient of thermal expansion (measured).

Table 1: Temperature-Independent Thermo-Mechanical Properties of Spring Steel (Print Bed).

Property	Value	Unit
Density	7.85	g/cm3
Young's Modulus	190	GPa
Poisson's Ratio	0.29	-
Yield Strength	525	MPa
Thermal Conductivity	52	W/(m·K)
Coefficient of Thermal Expansion	12	µm/(m·K)
Specific Heat Capacity	470	J/(kg·K)
Solidus Temperature	900	°C

Thin-walled cubes were printed on a PRUSA MK4 using a 0.4 mm nozzle at 180 °C, with a bed temperature of 50 °C, fixed ambient temperature at 25 °C, 0.2 mm layer height, 40 mm/s speed, and no cooling fan. After printing, cubes were coated with 3D scanning spray and scanned using the ARTEC Space Spider (0.05 mm accuracy). At least 1200 frames were captured per cube and processed in ARTEC Studio 18, including alignment, noise removal, fusion, and mesh optimization. The final 3D scans had a resolution of 0.1 mm. Warpage was assessed by comparing the scanned geometries to the original CAD models.

3.2 Simulation approach of thin-walled cube printing

The CAD models of the printed cube were converted to meshes for FE analyses. The layer thickness was set to 0.2 mm as discussed below in the printing process, resulting in 100 layers for the 20 mm cube and 200 layers for the 40 mm cube. Within each layer, each bead was represented as a single event. The bead width was divided into four mesh elements, while the bead thickness was set equal to the height of one mesh element. This resulted in mesh elements with dimensions of 0.1 mm x 0.1 mm x 0.2 mm, as shown in **Fig. 6a**. A mesh sensitivity analysis was conducted by reducing the mesh element thickness to 0.1 mm and 0.05 mm.

The substrate, simulating the PRUSA FDM printer bed, was modeled as a 1.3 mm thick deformable cuboid. Partition lines enabled a node-to-surface tie constraint with the printed cube and facilitated mesh alignment with the cube's first layer to minimize convergence issues. A uniform hexahedral mesh was used for the cube, while a coarser tetrahedral mesh was applied to the substrate to reduce computational time without sacrificing accuracy, as shown in **Fig. 6b**.

The thermal model assigned a uniform activation temperature of 150 °C to each mesh element, with a Goldak heat source (260 mW) raising the bead center to 180 °C. The print bed was set to 50 °C, with one side fixed at this temperature as a boundary condition. Black PLA's

emissivity was set to 0.92, and a film coefficient of 20 W/(m²·K) modeled free convection. A 0.1 s ramping coefficient was used to gradually introduce thermal strains and avoid convergence issues (**Fig. 6c**). Structurally, the print bed's bottom surface was fully constrained to simulate magnetic attachment to the printer chassis, accurately reflecting mechanical conditions during printing.

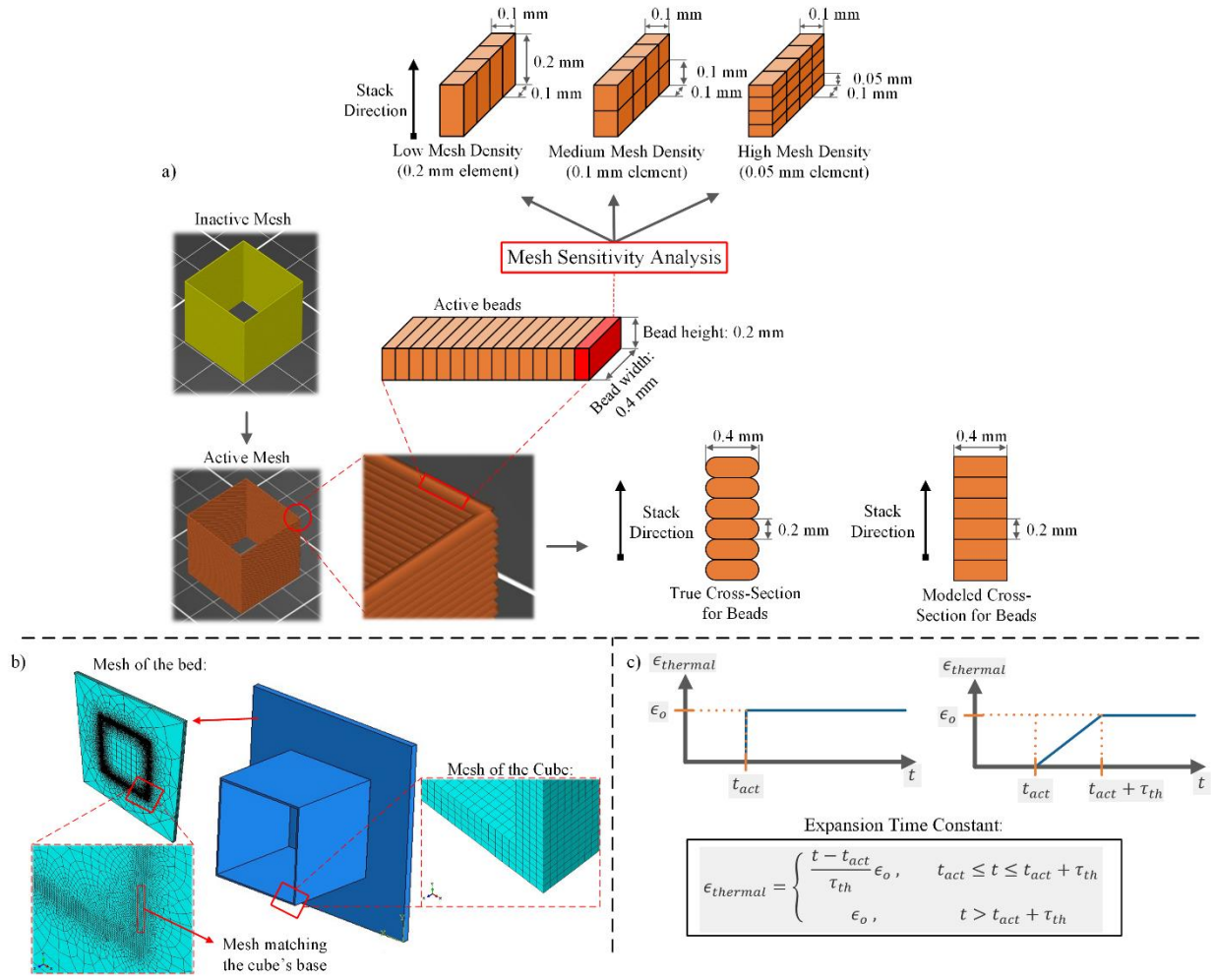


Figure 6: (a) Simulated approach modeling and meshing the bead's cross-section, (b) the simulated assembly for the FDM process along with the assigned part meshes, and (c) ramping of instantaneous thermal expansion over a time constant.

3.3 Validation of thin-walled cube printing

Simulations were conducted for the 20 mm and 40 mm thin-walled cubes, using three different mesh densities. When comparing the experimental displacement with simulated values,

shown in **Fig. 7**, the displacement decreases with increasing mesh density and saturates at a value lower than the experimentally measured value. For both cubes, two meshes per layer thickness are adequate to represent the experimental result. For this optimal mesh density, the simulated warpage for the 20 mm cube is 0.624 mm, which closely matches the experimentally measured value of 0.66 ± 0.05 mm. In the case of the 40 mm cube, the simulated warpage is 1.316 mm, slightly outside the experimental tolerance range of 1.39 ± 0.05 mm.

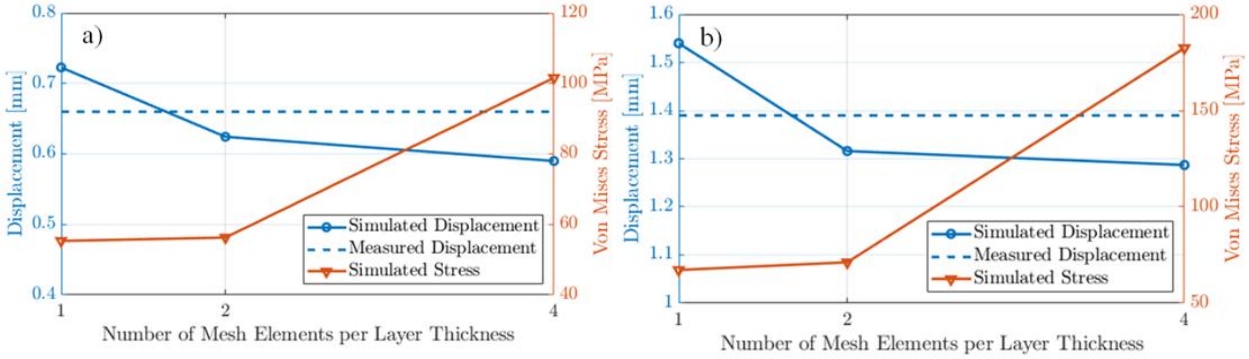


Figure 7: Variation of maximum displacement values for the investigated mesh densities (a) 20 mm and (b) 40 mm thin-walled cubes**.**

The values and locations of maximum displacements were compared between simulation and experiment. The experimentally measured warpage maxima, with a tolerance of 0.05 mm, was used as a reference for the true displacement values, as shown in **Fig. 8**. The simulation and experiment show good agreement in terms of the overall deformed shape and the magnitude of the warpage of the thin-walled cube. However, a discrepancy was observed regarding the direction of the wall warpage. In the simulation, all walls exhibit out-of-plane bending toward the center of the cube. In contrast, the experimental results indicate that two opposite walls warp toward the center, while the other two warp away from the center. This difference may be due to the snap-through behavior leading to an abrupt change in the warpage direction as the beads cool down. The vertical motion of the hot end when switching between layers leads to the deposition of small beads due to

oozing that is not captured in the simulation. This effect is noticeable at the corner where the nozzle switches between layers, resulting in a small agglomeration that is absent in the other three corners.

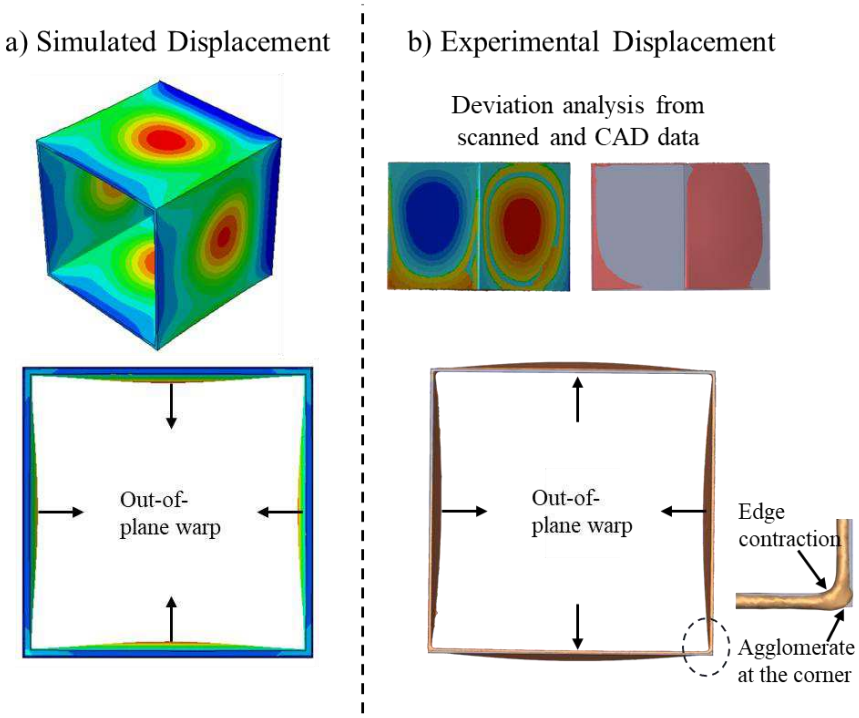


Figure 8: (a) Simulated displacement in ABAQUS along with a top view, and (b) deviation analysis for the reverse-engineered model and its top view.

The final displacement and von Mises stress distributions for both the 20 mm and 40 mm cubes are shown in **Fig. 9**. In the case of the 40 mm cube, the stress evolution follows a similar pattern to the 20 mm cube, but with a maximum von Mises stress of around 71.26 MPa at the corners, which is larger than the yield stress of PLA, shown in **Fig. 5**. This higher stress magnitude results from the larger thermal gradients along the inter-layer direction during the material deposition. The asymmetric tension-compression stress profile, driven by warping in the walls, is doubled in the 40 mm cube. This is due to the longer printing time for each layer, exposing the top surface of the bead to the convective boundary condition for a longer period before the next bead is deposited, resulting in high temperature fluctuations and gradients. The increased deflection in the 40 mm cube also shows edge warp, which is absent in the 20 mm cube.

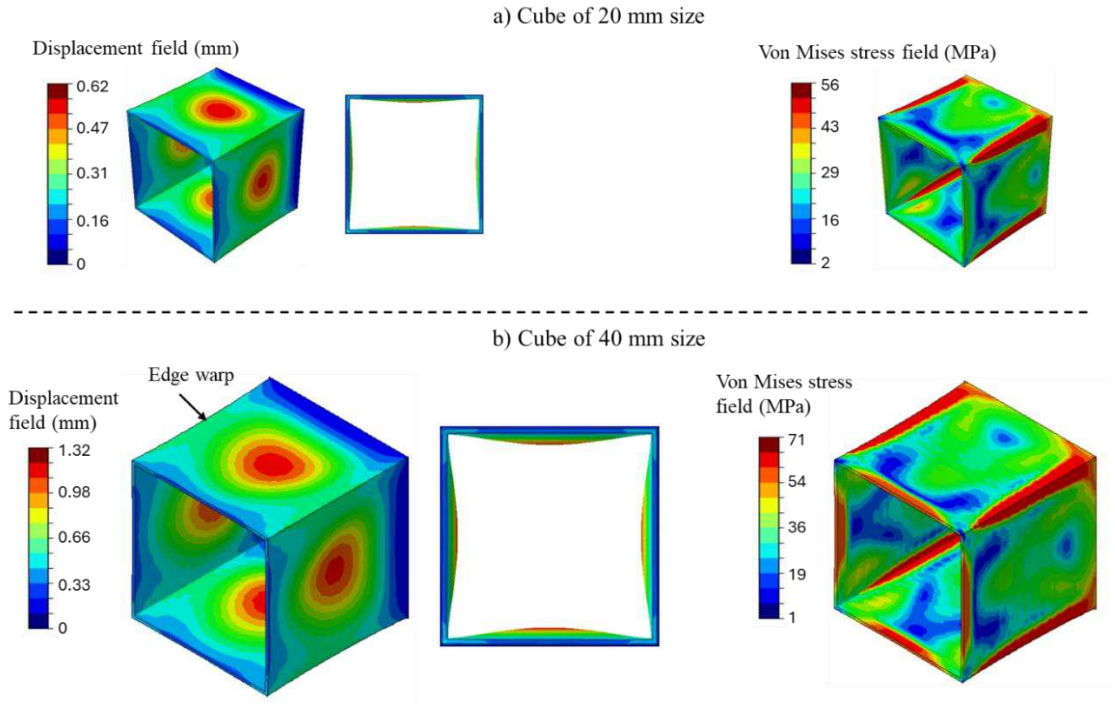


Figure 9: Displacement and (b) von Mises for (a) 20 mm cube and (b) 40 mm cube at the end of printing.

The accumulation of stress and the resulting displacements can be better understood by examining the temporal and spatial evolution of temperature during the depositions. For the 20 mm cube, as illustrated in **Fig. 10**, a recently deposited bead exhibits the highest heat flux in the form of conducted heat from the preceding layer. In the long term, the bead's temperature follows a typical decay pattern observed in transient heat convection processes, gradually dropping as it cools. However, when a new bead is deposited on top of a cooler layer, inter-layer reheating occurs due to the large temperature gradients between the newly activated bead and the cooler layers beneath it. This reheating effect is noticeable in the two preceding layers for each new bead deposited. By the time the third preceding layer is reached, no significant temperature gradient remains, as the heat conducted along the inter-layer direction is either dissipated through convection or stored as thermal energy in the layers. In contrast, for the 40 mm cube, the inter-layer reheating effect is evident over four preceding layers due to the larger temperature gradient

along the inter-layer direction, which is a result of the extended cooling time caused by the longer printing duration for each layer. These observations are consistent with experimentally measured results and have been reported in the work of Zhang et al. (2022), supporting the validity of the simulated temperature evolution and its influence on stress accumulation and warpage.

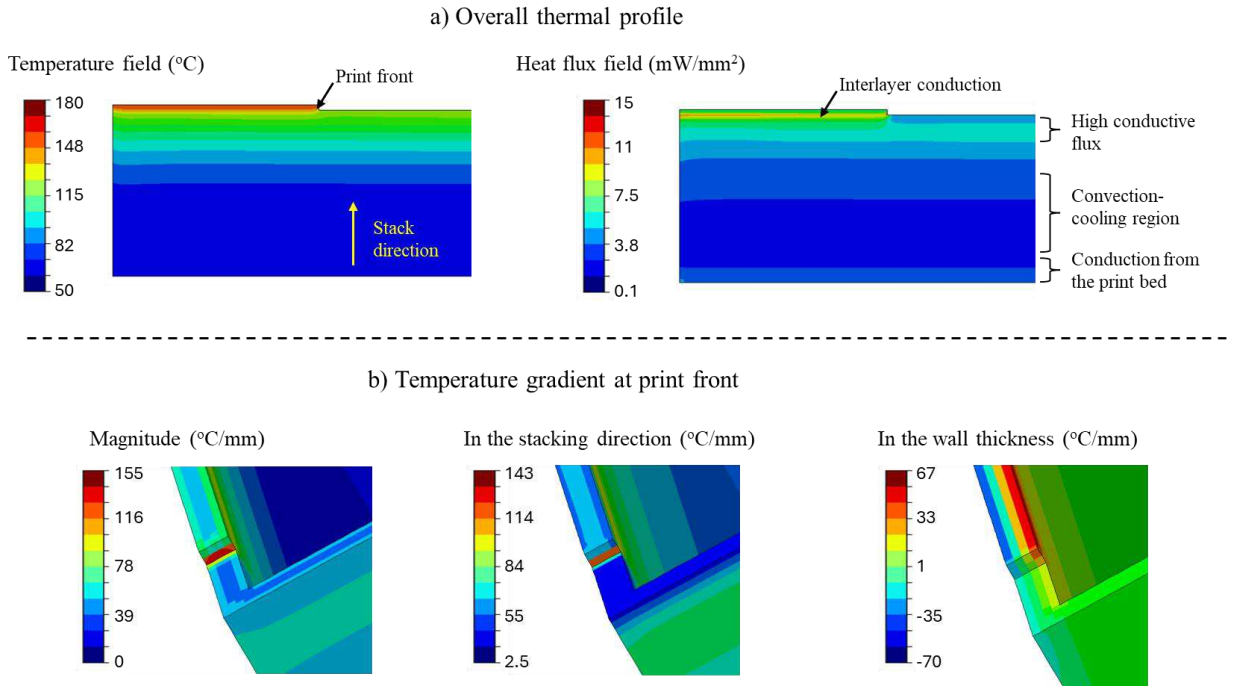


Figure 10: (a) Temperature and heat flux profile upon the activation of a bead (time = 80.25 seconds), and (b) temperature gradient components along the bead's width and thickness (time = 80.45 seconds).

3.4 Parametric studies of the influence of printing factors on shape distortion

The 20 mm cube was selected to study the effect of varying printing parameters (listed in **Table 2**) one at a time on shape distortion. The film coefficient was varied to control the convective heat flux. Experimentally, the lower film coefficient corresponded to no cooling (free convection), while the higher film coefficient represented the case where the cooling fan was turned on at 100% speed (forced convection). The ambient temperature (t_∞) for the convection and radiation processes was varied. This condition was experimentally reproduced by printing the cube inside a closed enclosure, where a temperature sensor was used to monitor and maintain the temperature

of the enclosure over time. Two sizes of bead dimensions (wall thickness) were studied to represent the different nozzle diameters. The number of mesh elements per layer thickness is kept constant at 2. This change was physically reproduced by installing a 0.6 mm nozzle on the 3D printer. Finally, a path-planning printing direction that alternated the hot end motion between clockwise (CW) and counterclockwise (CCW) for each subsequent layer was considered. The effect of these parameter variations on warpage displacement and von Mises stress is summarized in **Fig. 11** and discussed below.

Table 2: Parameters considered in parametric studies

Parameters	Values
Film coefficient (W/(m²·K))	20 to 300
Ambient temperature (°C)	25 to 50
Print bed temperature (°C)	50 to 25
Nozzle temperature (°C)	180 to 220
Printing speed (mm/s)	100 and 40
Bead dimension (mm)	0.4 and 0.6
Printing direction	Clockwise and counterclockwise

Changing the film coefficient to 300 W/(m²·K) reduces the warpage, as demonstrated by the simulated displacement of 0.56 mm near the center of the wall and experimental displacement of 0.43 ± 0.05 mm. Forced convection occurred primarily around the hot end, as the cooling fan was physically attached to this area. When the cooling fan was active, the most recently deposited bead cooled more rapidly, reaching the temperature of the previously deposited layer more quickly, which minimized inter-layer conductive heat flux. This cooling effect reduced the conductive heat transfer between layers, which controls thermal gradients. A higher film coefficient increased temperature gradients during the deposition of each new layer, leading to a more pronounced inter-layer reheating and rapid stress accumulation. The maximum stress was reduced by 10 MPa when a higher film coefficient was used, indicating faster heat dissipation from larger thermal gradients.

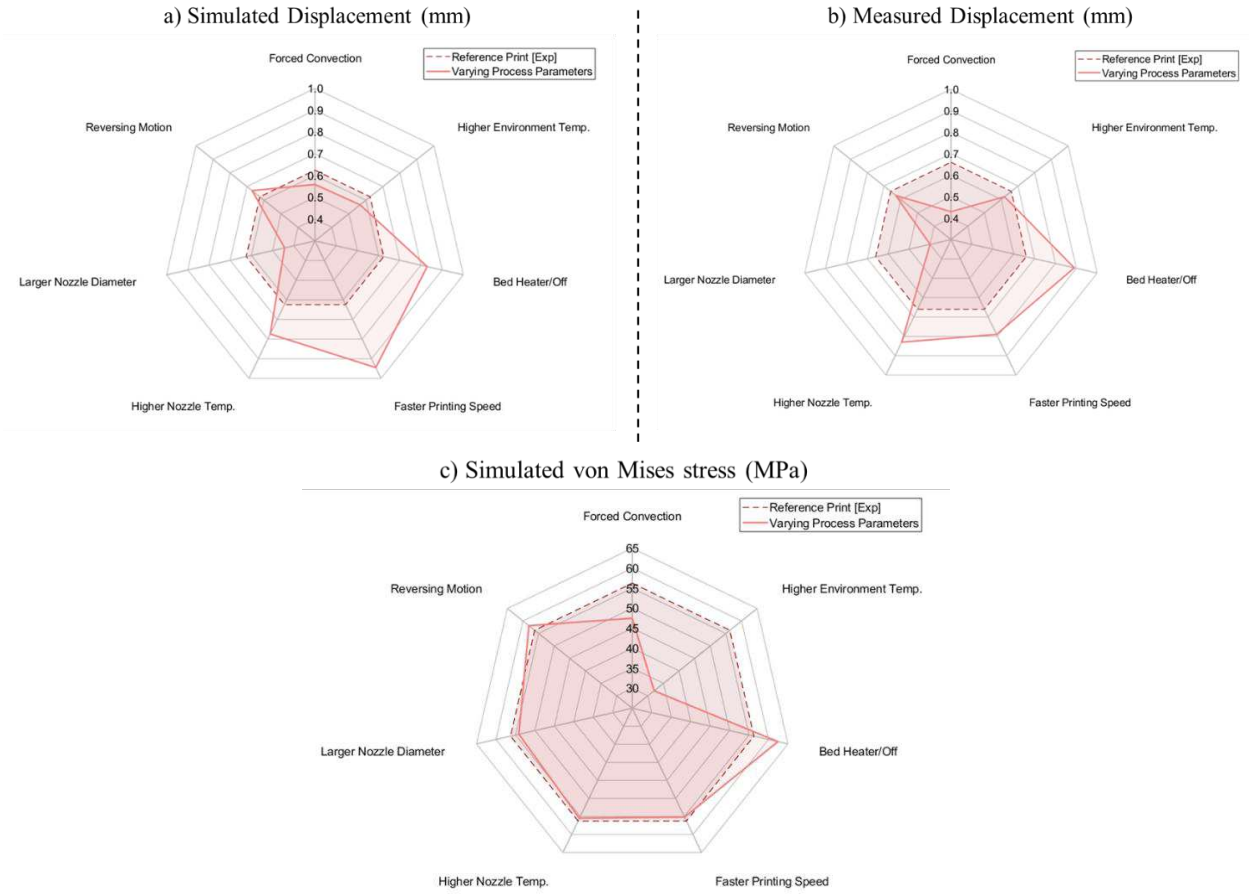


Figure 11: Radar charts illustrating the effect of varying process parameters with respect to the reference run for: (a) simulated and (b) measured maximum displacements, and (c) simulated maximum stress

Raising the ambient temperature creates a more uniform thermal profile across the printed layers by reducing heat loss through convection and radiation. Such gradual cooling helps to prevent large temperature gradients, which minimizes the risk of high thermal stresses, thereby reducing the warping. Notably, printing in a heated environment at ambient temperature to 50 ºC results in the lowest von Mises stress, with a maximum of 32 MPa. The corresponding simulated displacement is 0.57 mm, which is close to the experimental measurement of 0.62 ± 0.05 mm.

Reducing the print bed temperature to 25 ºC, the simulated and measured displacements are 0.95 and 0.89 ± 0.05 mm, respectively, which are notably higher than those observed with a

heated bed. An unheated bed creates larger thermal gradients for the layers closer to the bed, inducing higher thermal residual stress at the corners and causing them to detach from the bed. Although this detachment phenomenon is not explicitly modeled in the simulation, von Mises stresses as high as 62.44 MPa are observed, exceeding the yield strength of PLA.

Increasing the printing speed to 100 mm/s results in a 0.13 mm increase in warpage, with no significant effect on thermal stress. At higher speeds, the rapid deposition of a hot bead onto a relatively warm layer reduces the temperature gradient and the inter-layer reheating effect. The average temperature of the layers remains higher, which explains the increased warpage. The increase in print speed negatively impacted the surface quality of the part, as rougher surfaces with more visible layer lines were observed.

Increasing the nozzle temperature to 220 °C introduces additional heat into the printed part, extending the range of temperature drop during the cooling phase. This results in larger thermal fluxes and gradients, which are expected to increase both displacement and stress values. While a notable increase in displacement was observed, the von Mises stresses were not significantly affected in the simulation.

Increasing the bead width to 0.6 mm and the thickness to 0.3 mm reduces the print time by allowing more material to be extruded. However, this increase in bead dimensions results in greater surface roughness. Depositing thicker layers concentrates more thermal energy in each pass, causing the outer surface to cool faster than the center of the bead. In terms of simulated displacement, a reduction of 0.22 mm is observed, as larger beads are more rigid and less prone to out-of-plane warpage. Larger beads also promote more effective heat dissipation, particularly around corners and sharp edges, reducing the risk of localized stress concentration and improving the overall dimensional stability of the printed part.

Both simulation and experimental results indicate minimal changes in displacement when altering the printing direction. The reference displacement is 0.66 mm, while the simulated and measured values are 0.67 mm and 0.63 ± 0.05 mm, respectively. When the hot end reverses direction, the thermal gradient is minimal but increases along the bead's axis as surrounding areas cool. This gradual gradient helps reduce thermal shock and preserve structural integrity. In larger prints, greater interlayer gradients lead to higher heat flux and stress buildup, suggesting the printing algorithm's impact becomes more significant at larger scales.

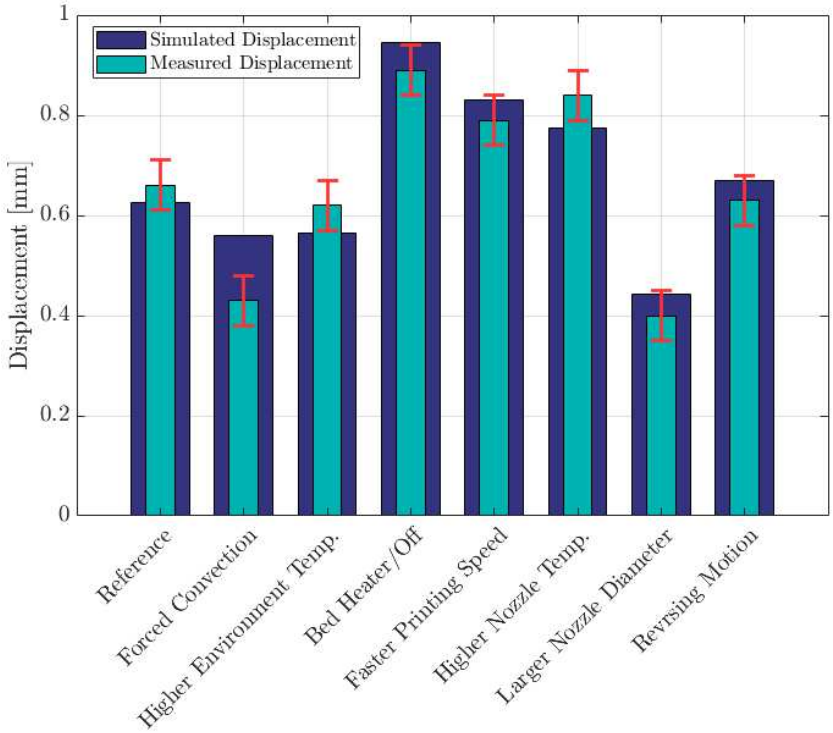


Figure 12: Bar chart comparison for the simulated and measured warpage at the center of the walls.

Figure 12 summarizes the warpage from the above parametric studies, comparing the experimental and simulation results. The results show several optimized printing parameters to reduce the warpage in thin-walled cubes. It is seen that the forced convection and nozzle diameter have a significant impact on the warping displacement. As an example, the printed cubes with and

without forced convection are shown in **Fig. 13**, highlighting the reduction in shape distortion with forced convection. Heat conduction through the layers is not sufficient to dissipate heat during printing. We demonstrate the use of 3D printing simulation to determine proper printing parameters to alleviate wrinkling and warpage in the 3D printed thin-walled cubes.

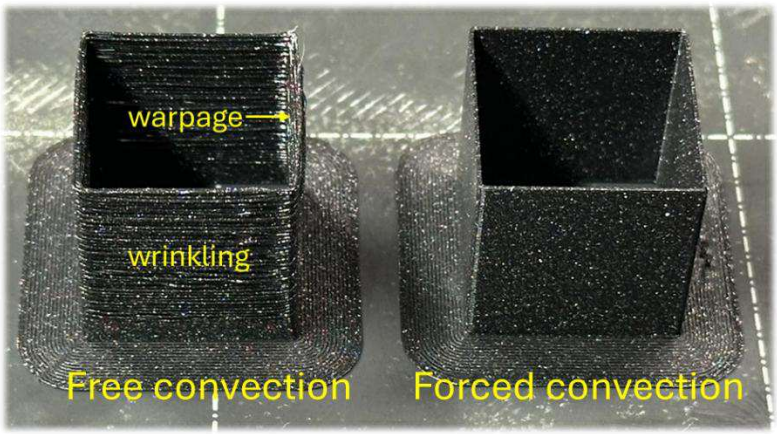


Figure 13: 3D printed thin-walled cube with and without forced convection

4. Printing of Thin-walled Tessellated Tubes

To further demonstrate the use of printing simulation in guiding proper printing parameters, we explore the fabrication of a thin-walled tessellated tube, depicted in **Fig. 14**. A unique design principle of a tessellated tube is attributed to its congruent geometry with alternating concave and convex arcs along opposing edges. The design is inspired by an apple core tessellation and historically found in woodblock prints of Katsushika Hokusai (1760–1849). Multiple tessellated tubes can be assembled to create an interlocked structure without any adhesive or connection (Grünbaum and Shephard 1987; Dyskin et al., 2001; Estrin et al., 2011). The concavo-convex surface curvature distributes contact forces across a larger interface area than flat-faced tubes, reducing stress concentrations and enhancing load-bearing performance as measured by stiffness, strength, and stability (Estrin et al., 2011). The tessellated tubes are beneficial for applications where reversibility, material efficiency, and resistance to multi-directional loading are required.

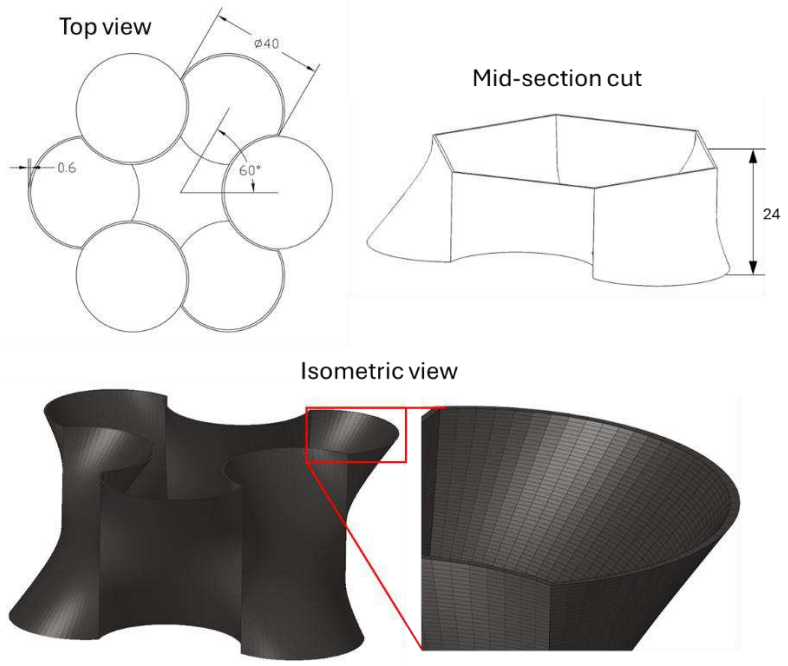


Figure 14: A thin-walled tessellated tube: CAD model of top view and mid-section slice, unit is in mm, (Top) and Isometric view and meshed elements (Bottom)

We consider a tessellated tube of 48 mm height and 0.6 mm wall thickness having opposite concave and convex circles, each with a diameter of 40 mm. The tessellated tube shows an overhanging wall with a transition from a concave to a convex surface across the height of varying degrees of curvature. At the mid-surface, where the transition occurs, it has zero curvature. To be compatible with the event series generated by the G-code, shown in **Fig. 4**, we use a uniform meshing through the height and mesh the outer and inner surfaces of the tube separately using a 2D quad mesh in Altair HyperMesh. To generate 3D meshes for the simulation, we connect the outer and inner surfaces and select elements through the thickness based on the contour loops being printed in the FDM, as shown in **Fig. 14**.

For the simulation, we mesh the tessellated tube to map the actual printing process with a 0.6 mm nozzle and a layer height of 0.3 mm, resulting in a total of 160 layers. In total, we model the tessellated tube with 38,400 C3D8 brick elements. To further validate our study on the

influence of film coefficient in **Section 3**, two sets of simulations with a film coefficient of 20 W/(m²·K) mimicking the free convection and another film coefficient of 300 W/(m²·K) mimicking the forced convection with 100% fan speed are performed. In both cases, nozzle temperature of 180 °C, bed temperature of 50 °C, and ambient temperature of 25 °C are considered.

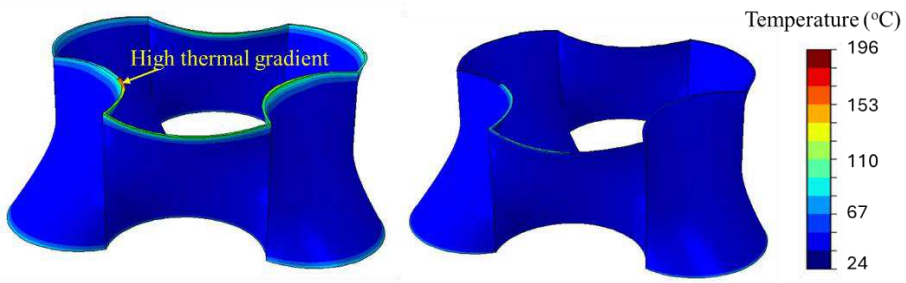


Figure 15: Temperature profile during printing with free convection (Left) and forced convection (Right) conditions

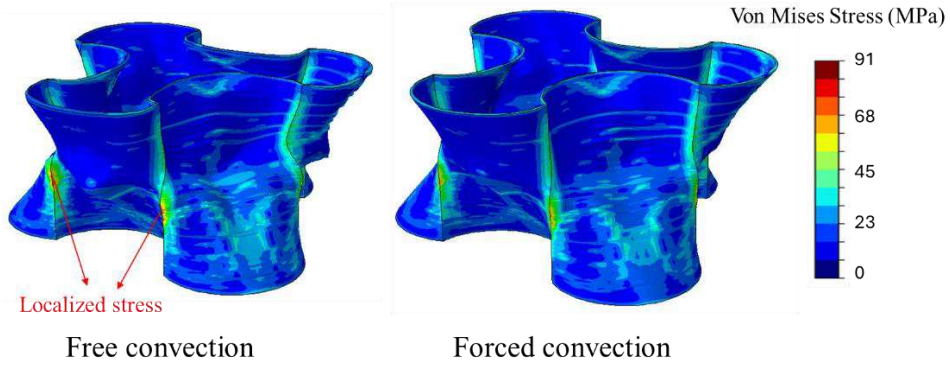


Figure 16: Stress profile after printing and cooling down from free convection (Left) and forced convection (Right) conditions

Figure 15 shows the simulated temperature profile during printing (at 815 seconds), highlighting the influence of free and forced convection on the thermal gradient. The forced convection condition results in a more uniform temperature. A high thermal gradient is seen at the deposited region in the free convection condition. The thermal gradient results in the formation of residual (thermal) stress, which is more pronounced at the sharp corners of the segments where the transitions from concave to convex surface take place, as depicted in **Fig. 16**. In both cases, residual

stress is seen after the cooling down to room temperature at 25 °C. Reducing the thermal gradient minimizes the magnitude of residual stress. As seen in the stress profile, the stress magnitude at the localized regions exceeds the yield strength of the PLA, which is 50 MPa at 25 °C (shown in **Fig. 5**), indicating that damage might occur in the printed tessellated tube. The simulation can offer insight into the thermal stress formation during printing and the development of residual stress after printing, which is crucial for determining the load-bearing ability of the 3D printed objects.

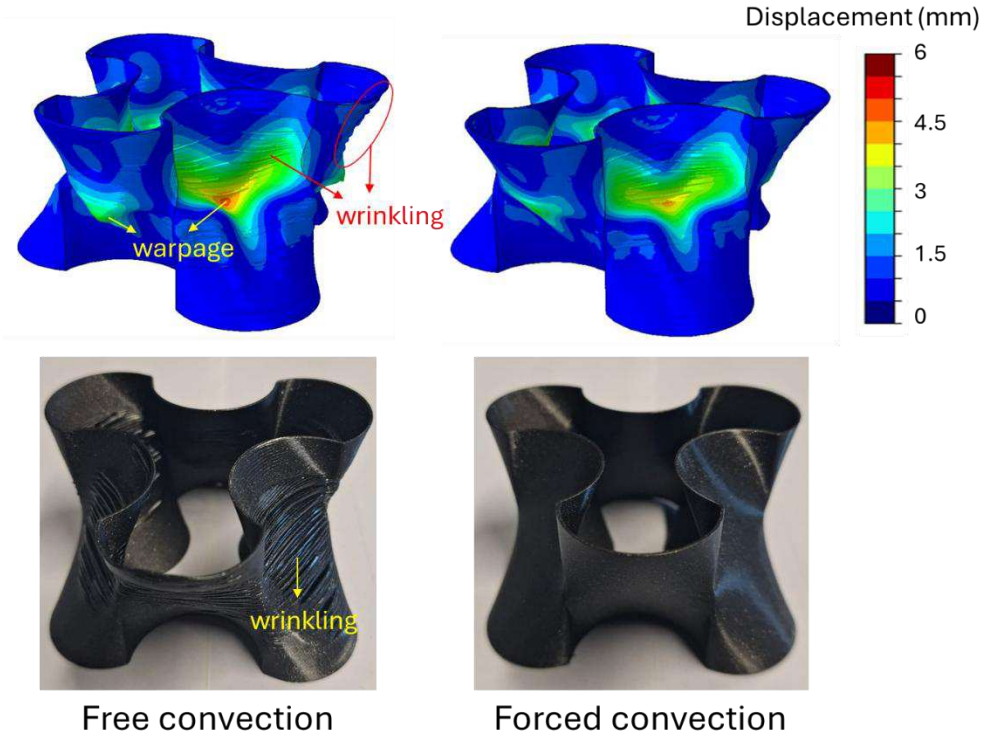


Figure 17: Displacement profile after printing and cooling down, comparing simulation (Top) and experiment (Bottom) with free convection (Left) and forced convection (Right)

The corresponding displacements from the free and forced convection printing conditions are depicted in **Fig. 17**. Without forced convection, poor heat conduction within layers causes longer solidification, leading to deformations under the weight of subsequent deposited layers. The printing simulation can predict the severe wrinkling and its location observed in the printed tessellated tube. In both cases, warpage displacement, which indicates shape distortion, takes place

in the printed tessellated tube. However, with forced convection, its severity can be minimized. To assess shape distortions, the root mean square (RMS) of deviation from the CAD model was determined using the ARTEC Space Spider. The RMS value of 0.66 mm was found under free convection, and 0.39 mm under forced convection.

5. Conclusion and Future Directions

The digital twin of FDM thermoplastic printing that maps the real printing process, including layer-by-layer deposition characteristics of molten polymers as defined by the printing parameters and cooling down process, has been used to understand the formation of residual stress and shape distortion of 3D printed thin-walled complex geometries. To facilitate the FDM digital twin, we developed a trajectory-based motion of the hot end through a series of deposition events, which track time and positions of deposited and solidified materials and field variables, i.e., temperature, displacement, and stress. The simulation also accounts for the solidification process and irreversible material properties through incorporating temperature-dependent thermal and elastic-plastic mechanical properties. We also presented a 3D scan of the printed objects to evaluate warpage across the entire printed surface, not just the distortion at a few discrete points.

Using the simulation, we have identified printing parameters that have pronounced effects on the temporal and spatial temperature variations during printing, and the formation of shape distortion. The temperature difference occurs between the top (free) and bottom (adjacent to already deposited bead) surface of the bead that is being deposited and the inner and outer side of the printed wall due to multiple convection, radiation, and conduction, leading to an asymmetric solidification process across the bead and hence warpage. Continuously depositing layers on still solidifying printed segments induces deformations on these printed segments, resulting in wrinkling. Longer printing time for each layer in a larger specimen causes the top surface of the

bead to remain exposed to the convective boundary condition for a longer period before the next bead is deposited, resulting in larger temperature fluctuations and steeper gradients. The higher conduction rates and lower convection rates around the sharp edges/corners in both cube and tessellated tube slow down the cooling process and prolong the time required for the material to reach ambient temperature. The heat accumulation in areas near sharp edges causes high stress in the stacking direction, which potentially results in layer delamination.

Guided by the digital twin, we performed thermal management during printing by allowing fast cooling through forced convection and assessed its effectiveness in mitigating wrinkling and warpage. Thin-walled cubes and tessellated tubes have been evaluated simultaneously in real and digital printing under both free and forced convection conditions, which correspond to conditions without and with cooling intervention, respectively. The digital printing can predict the wrinkling and warpage observed in the real printed structures. The digital printing can also determine the formation and distribution of residual stress, which is limited in real printing.

This study provides insights into the fundamental mechanisms that cause shape distortion in FMD printed thin-walled complex geometries and the ability of tuning printing parameters to mitigate residual stress and shape distortion. Future studies can leverage the digital twin of FDM printing to develop databases of temperature, stress, and displacement profiles as a function of time and space of 3D printed objects of various complex shapes, polymers, and printing parameters to guide the real printing.

Funding Source: The portions of the research reported in this publication were supported by the Qatar Research Development and Innovation Council under grant [NPRP14C-0920–210017] and the US National Science Foundation under grant CMMI-2013696.

References

1. "AISI 9260 61SICR7 1.7108 spring steel: Fushun Special Steel," Fushun Special Steel Co., Ltd. - Professional Supplier of Special Steel, and Manufacturer of Tool Steel | manufacturer of tool steel, stainless steel, nickel alloy, alloy steel, https://www.fushunspecialsteel.com/aisi-9260-61sicr7-1-7108-spring-steel/ (accessed Sep. 20, 2024)
2. Al Rasid A and Koc M, "Fused filament fabrication process: A review of numerical simulation techniques" Polymers, 13, 3534, 2021
3. N. An et al., "Implementation of Abaqus User Subroutines and plugin for thermal analysis of powder-bed electron-beam-melting additive manufacturing process," Materials Today Communications, vol. 27, p. 102307, Jun. 2021. doi:10.1016/j.mtcomm.2021.102307
4. Armillotta, A.; Bellotti, M.; Cavallaro, M, Warpage of FDM parts: Experimental tests and analytic model," Robot. Comput. Integr. Manuf. 2018, 50, 140–152
5. S. Bhandari and R. A. Lopez-Anido, "Discrete-event simulation thermal model for extrusion-based additive manufacturing of PLA and ABS," Materials, vol. 13, no. 21, p. 4985, Nov. 2020. doi:10.3390/ma13214985
6. Brenken B, Barocio E, Favaloro A, Kunc V, and Pipes RB, "Fused filament fabrication of fiber-reinforced polymers: A review" Additive Manufacturing, 21, pp. 1-16, 2018
7. Brenken B, Barocio E, Favaloro A, Kunc V, and Pipes RB, "Development and validation of extrusion deposition additive manufacturing process simulations" Additive Manufacturing, 25, pp. 218-226, 2019
8. Chaoui K, Chudnovsky A and Moet A, "Effect of residual stress on crack propagation in MDPE pipes" J. Material Science, 22, pp. 3873-3879, 1987
9. G. Chen et al., "Simulating and predicting the part warping in fused deposition modeling by thermal–structural coupling analysis," 3D Printing and Additive Manufacturing, vol. 10, no. 1, pp. 70–82, Feb. 2023. doi:10.1089/3dp.2021.0119
10. Costa SF, Duarte FM, and Covas JA, "Estimation of filament temperature and adhesion development infused deposition techniques" J. Materials Processing Technology, 245, pp. 167-179, 2017
11. Duty C, Ajinjeru C, Kishore V, Compton B, Hmeidat N, Chen X, Liu P, Hassen AA, Lindahl J, Kunc V, "What makes a material printable? A viscoelastic model for extrusion-based 3D printing of polymers" J. Manufacturing Processes, 35, pp. 526-537, 2018
12. Dyskin, A. V., Estrin, Y., Kanel-Belov, A. J., & Pasternak, E. (2001). A new concept in design of materials and structures: Assemblies of interlocked tetrahedra. Scripta Materialia*,* 44(12), 2689–2694
13. Estrin, Y., Dyskin, A. V., & Pasternak, E. (2011). Topological interlocking as a material design concept. Materials Science and Engineering*: C,* 31(6), 1189–1194
14. El Moumen A, Tarfaoui M, Lafdi K, "Modelling of the temperature and residual stress fields during 3D printing of polymer composites" The International Journal of Advanced Manufacturing Technology, 104:1661–1676, 2019
15. Garzon-Hernandez S, Garcia-Gonzalez D, Jerusalem A, and Arias A, "Design of FDM 3D printed polymers: An experimental-modelling methodology for the prediction of mechanical properties" Materials and Design, 188, 108414, 2020
16. Grünbaum, B., & Shephard, G. C. (1987). Tilings and Patterns. W. H. Freeman
17. "Iron alloy," MakeItFrom.com, https://www.makeitfrom.com/material-properties/ASTM-A227-Spring-Steel (accessed Sep. 20, 2024)

18. Jiang B, Chen Y, Ye L, Change L, and Dong H, “Residual stress and warpage of additively manufactured SCF/PLA composite parts” Advanced Manufacturing: Polymer & Composites Science, 9:1, 2171940, 2023

19. Hakimian E and Sulong AB, “Analysis of warpage and shrinkage properties of injection-molded micro gears polymer composites using numerical simulations assisted by the Taguchi method” Materials and Design, 42, pp. 62-71, 2012

20. Hornberger LE and Devries KL, “The effect of residual stress on the mechanical properties of glassy polymers” Polymer Engineering and Science, 27 (19), pp. 1473-1478, 1987

21. M. Kaavessina, I. Ali, and S. M. Al-Zahrani, “The influences of elastomer toward crystallization of poly(lactic acid),” Procedia Chemistry, vol. 4, pp. 164–171, 2012. doi:10.1016/j.proche.2012.06.023

22. Y. Li et al., “Microstructural evolution and mechanical properties of 60Si2CrVNb spring steel under quenching-tempering heat treatment process,” Journal of Materials Research and Technology, vol. 25, pp. 6829–6842, Jul. 2023. doi:10.1016/j.jmrt.2023.07.099

23. J. Luo, Q. Luo, G. Zhang, Q. Li, and G. Sun, “On strain rate and temperature dependent mechanical properties and constitutive models for additively manufactured polylactic acid (PLA) materials,” Thin-Walled Structures, vol. 179, p. 109624, Oct. 2022. doi:10.1016/j.tws.2022.109624

24. A. A. Mishra, A. Momin, M. Strano, and K. Rane, “Implementation of viscosity and density models for improved numerical analysis of melt flow dynamics in the nozzle during extrusion-based additive manufacturing,” Progress in Additive Manufacturing, vol. 7, no. 1, pp. 41–54, Jul. 2021. doi:10.1007/s40964-021-00208-z

25. Nascimento, E.J.G., dos Santos Magalhães, E. & dos Santos Paes, L. A literature review in heat source thermal modeling applied to welding and similar processes. Int J Adv Manuf Technol 126, 2917–2957 (2023). https://doi.org/10.1007/s00170-023-11253-z

26. G. C. Nzebuka, C. O. Ufodike, A. M. Rahman, C. M. Gwynn, and M. F. Ahmed, “Numerical modeling of the effect of nozzle diameter and heat flux on the polymer flow in fused filament fabrication,” Journal of Manufacturing Processes, vol. 82, pp. 585–600, Oct. 2022. doi:10.1016/j.jmapro.2022.08.029

27. A. Özen, G. Ganzosch, C. Völlmecke, and D. Auhl, “Characterization and multiscale modeling of the Mechanical Properties for FDM-printed copper-reinforced PLA composites,” Polymers, vol. 14, no. 17, p. 3512, Aug. 2022. doi:10.3390/polym14173512

28. D. Popescu, A. Zapciu, C. Amza, F. Baciu, and R. Marinescu, “FDM process parameters influence over the mechanical properties of polymer specimens: A Review,” Polymer Testing, vol. 69, pp. 157–166, 2018. doi:10.1016/j.polymertesting.2018.05.020

29. A. Prada et al., “Nanoparticle shape influence over poly(lactic acid) barrier properties by molecular dynamics simulations,” ACS Omega, vol. 7, pp. 2583–2590, 2022. doi:10.1021/acsomega.1c04589

30. A. Ronca et al., “A comparative study for material selection in 3D printing of scoliosis back brace,” Materials, vol. 15, no. 16, p. 5724, Aug. 2022. doi:10.3390/ma15165724

31. T. Santos et al., “Insights into temperature simulation and validation of fused deposition modeling processes,” Journal of Manufacturing and Materials Processing, vol. 7, no. 6, p. 189, Oct. 2023. doi:10.3390/jmmp7060189

32. I. J. Solomon, P. Sevvel, and J. Gunasekaran, “A review on the various processing parameters in FDM,” Materials Today: Proceedings, vol. 37, pp. 509–514, 2021. doi:10.1016/j.matpr.2020.05.484

33. Spoerk M, Gonzales-Gutierrex J, Lichal C, Cajner H, Berger-Weber G, Schuschnigg S, Cardon L, and Holzer C, “Optimisation of the Adhesion of Polypropylene-Based Materials during Extrusion-Based Additive Manufacturing” Polymers, 10, 490, doi:10.3390/polym10050490, 2018

34. Spoerk M, Holzer C, and Gonzales-Gutierrex J, “Material extrusion-based additive manufacturing of polypropylene: A review on how to improve dimensional inaccuracy and warpage” J. Applied Polymer Science, 48545, pp. 1-16, 2020

35. Sreejith P, Kannan K, and Rajagopal KR, “A thermodynamic framework for additive manufacturing, using amorphous polymers, capable of predicting residual stress, warpage and shrinkage” Int. J. Engineering Science, 159, 103412, 2021

36. C. O. Ufodike and G. C. Nzebuka, “Investigation of thermal evolution and fluid flow in the hot-end of a material extrusion 3D printer using melting model,” Additive Manufacturing, vol. 49, p. 102502, Jan. 2022. doi:10.1016/j.addma.2021.102502

37. D. Vaes, M. Coppens, B. Goderis, W. Zoetelief, and P. Van Puyvelde, “Assessment of crystallinity development during fused filament fabrication through fast scanning chip calorimetry,” Applied Sciences, vol. 9, no. 13, p. 2676, Jun. 2019. doi:10.3390/app9132676

38. Wang TM, Xi JT, and Jin Y, “A model research for prototype warp deformation in the FDM process” Int. J. Advanced Manufacturing Technology, 33, pp. 1087-1096, 2007

39. Xia H, Lu F, Dabiri S, and Tryggvason G, “Fully resolved numerical simulations of fused deposition modeling. Part I: fluid flow” Rapid Prototyping Journal, 24/2, pp. 463-476, 2018

40. Xia H, Lu F, and Tryggvason G, “Fully resolved numerical simulations of fused deposition modeling. Part II: solidification, residual stresses and modeling of the nozzle,” Rapid Prototyping Journal, 24/6, pp. 973-987, 2018

41. Xia H, Lu J, and Tryggvason G, “A numerical study of the effect of viscoelastic stresses in fused filament fabrication,” Computer Methods in Applied Mechanics and Engineering, 346, pp. 242-250, 2019

42. Xinhua, L.; Shengpeng, L.; Zhou, L.; Xianhua, Z.; Xiaohu, C.; Zhongbin, W, “An investigation on distortion of PLA thin-plate part in the FDM process,” Int. J. Adv. Manuf. Technol. 2015, 79, 1117–1126

43. Yardimci, M.A.; Hattori, T.; Guceri, S.I.; Danforth, S.C. “Thermal analysis of Fused Deposition,” In Proceedings of the 1997 International Solid Freeform Fabrication Symposium, Austin, TX, USA, 11–13 August 1997; pp. 689–698

44. J. Zhang et al., “Temperature analyses in fused filament fabrication: From filament entering the hot-end to the printed parts,” 3D Printing and Additive Manufacturing, vol. 9, no. 2, pp. 132–142, Apr. 2022. doi:10.1089/3dp.2020.0339

45. C. Zhou et al., “Temperature dependence of poly(lactic acid) mechanical properties,” RSC Advances, vol. 6, no. 114, pp. 113762–113772, 2016. doi:10.1039/c6ra23610c

Supplementary Files

This is a list of supplementary files associated with this preprint. Click to download.

- declarationofcompetinginterests.docx